Influence of spontaneous emission on a single-state atom interferometer

S. Beattie,[1] B. Barrett,[1] M. Weel,[1] I. Chan,[1] C. Mok,[1] S. B. Cahn,[2] and A. Kumarakrishnan[1]
[1]*Department of Physics and Astronomy, York University, Toronto, Ontario, Canada M3J 1P3*
[2]*Department of Physics, Yale University, New Haven, Connecticut 06511, USA*
(Received 12 September 2007; published 15 January 2008)

We have studied the effects of spontaneous emission (SE) on a single-state time domain atom interferometer (AI) that uses trapped Rb atoms. The AI uses two standing wave pulses separated by time T to produce an echo signal at time $2T$ due to interference between momentum states. We find that SE influences both the shape of the echo signal and its periodic time-dependent amplitude in a manner consistent with theoretical predictions. The results show that the time-dependent signal from the AI is related to the effective radiative decay rate of the excited state. We also present results that test theoretical predictions for several properties of the echo formation such as the variation in momentum transfer due to the change in the angle between the traveling wave components of the excitation pulses, strength of the atom-field interaction, and the effect of spatial profile of the excitation beams. These studies are important for realizing precision measurements of the atomic fine structure constant and gravity using this interferometer.

DOI: 10.1103/PhysRevA.77.013610 PACS number(s): 03.75.Dg, 37.10.De, 42.50.Md, 37.10.Vz

I. INTRODUCTION

Recent experiments using atom interferometers (AIs) have led to remarkable improvements in precision measurements [1]. Among the best known experiments in this category are atom interferometric measurements of the atomic fine structure constant [2,3], gravitational acceleration [4], rotation [5], and gravity gradients [6]. Experiments in the area of light-matter interactions have also provided interesting tests of quantum mechanics. These include numerous experiments with Bose-Einstein condensates (BEC) such as superradiance [7], efficient output coupling of BEC [8], and measurements of the effect of the index of refraction on the wave vector [9]. The work presented in [2–6] has relied on Raman interferometers that involve transitions between hyperfine ground states of trapped atoms whereas the experiments in [8,9] have used an AI that manipulates atoms in a single atomic ground state. A single-state AI was demonstrated in Ref. [10]. Subsequently, we have developed single-state AIs that work in both the time domain [11,12] and the frequency domain [13] for obtaining precise measurements of atomic recoil (related to the atomic fine structure constant α) and gravitational acceleration, g. An important challenge for the time domain measurements in Refs. [11,12] is to understand the effects of spontaneous emission (SE) on the signal shape. These effects can contribute to systematic shifts on the precision measurement.

The excitation scheme for the AI is shown in Fig. 1. It involves an off-resonant standing wave pulse applied at $t=0$ to diffract an atom into a superposition of momentum states separated by integer multiples of $2\hbar q$, as shown in Fig. 2. Here, $\hbar \equiv h/2\pi$, where h is Planck's constant and $\mathbf{q} \equiv \mathbf{k}_1 - \mathbf{k}_2$ is the difference in wave vectors between the traveling wave components (generally counterpropagating) of the standing wave excitation pulses. A second off-resonant standing wave pulse at $t=T$ results in momentum state interference and produces echoes in the vicinity of $t=2T, 3T, \ldots$. Figure 2 shows a subset of momentum states that interfere at $t=2T$. The echo at $t=2T$ is associated with a density modulation with a period $\lambda/2$ (where λ is the wavelength of the traveling wave components of the excitation pulses) in the atomic sample just before and after $t=2T$. A readout pulse is applied in the vicinity of $t=2T$ and the echo is detected by coherent backscattering from the density grating. This signal represents an average over the velocity distribution of the sample of trapped atoms. The echo envelope has a characteristic dispersion shape as shown in Fig. 2. The signal envelope shows that a density grating is present just before and after $t=2T$. The signal zero at $t=2T$ represents the recreation of the uniform density distribution that was present at $t=0$. The echo amplitude measured as a function of T exhibits a period $T_{\text{recoil}} = \pi/\omega_q$, where $\omega_q = \hbar q^2/2M$ is the atomic recoil

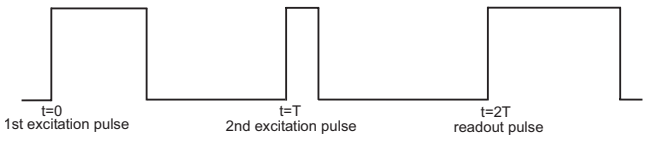

FIG. 1. Timing diagram for the single-state AI used in this work. Pulse durations of the first and second standing wave pulses are typically in the range 500–800 ns and 30–200 ns, respectively.

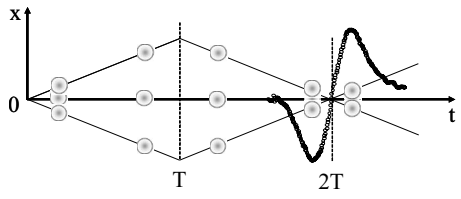

FIG. 2. Billiard ball representation of the momentum states associated with the interferometer. Only three possible trajectories $(0, \pm\hbar q)$ due to the first excitation pulse are shown. A subset of higher-order processes $(\pm 2\hbar q, \pm 3\hbar q$, etc.) can be rephased at $t=2T$, but only trajectories differing by $\hbar q$ contribute to the signal at $t=2T$. The echo envelope is also shown in the vicinity of $t=2T$ and its temporal width is inversely proportional to the velocity distribution. Here, the time interval between extrema is ~ 2 μs, $T \sim 1-30$ ms, and $T_{\text{recoil}} = \pi/\omega_q \sim 32$ μs.

frequency, and M is the atomic mass. The recoil period can be understood physically as the time taken for a wave packet traveling with recoil velocity $\hbar\mathbf{q}/M$ to move through one period $(\lambda/2)$ of the density grating. A precision measurement of $\hbar/M$ can be obtained by measuring the periodic echo amplitude as a function of the excitation pulse separation T and extracting the temporal separation between widely separated minima [10,11]. An advantage of the technique used in this work is that the periodic signal can be detected with 100% contrast. Although the time scale and precision associated with the experiment should be limited only by the transit time of the atoms through the region of interaction, in practice it is necessary to eliminate the effects of decoherence due to atomic collisions and background light. Magnetic field gradients also cause amplitude oscillations that must be eliminated [12]. An interesting aspect of this experiment is that the Doppler phases accumulated by the momentum states are canceled at the echo times. As a result the experiment does not rely on velocity selection. The primary benefit of cooling the sample is to extend the transit time.

Spontaneous emission during the excitation pulses results in a change in the shape of the echo envelope and induces an asymmetry in the periodic T-dependent echo amplitude. The change in the echo amplitude versus T is also associated with a temporal offset [10]. Understanding the impact of SE plays a crucial role in fitting the T-dependent signal and extracting ω_q. In this work, we present a calculation of the echo signal including the effect of SE and show that this theoretical model is effective in describing the echo envelope and T-dependent signal shape. A measurement of the effective radiative rate of the sample can be extracted from fits to the data. The effective rate shows the predicted dependence on the detuning of the standing wave pulses. The measured radiative rate exhibits a characteristic dependence on the duration of the second standing wave pulse. This rate asymptotically approaches the radiative rate for an isolated atom for sufficiently long interaction pulses. Using a numerical simulation involving the dressed state basis, we show that this effect is related to atomic motion in the periodic optical potential as well as in the spatial profile of the excitation beams. We also present studies of the T-dependent echo amplitude as a function of the strength of the atom-field coupling (pulse area), spatial profile of excitation beams, and momentum imparted to the atoms and compare with predictions.

The rest of the paper is organized as follows. In Sec. II we describe a calculation of the echo signal including the effect of SE during the pulses. Some of the details pertaining to manipulation of Bessel functions used in the calculation are presented in the Appendix. The experimental details are presented in Sec. III and a discussion of the data is given in Sec. IV. Finally, we compare the data with numerical simulations based on dressed states to understand the effective radiative rate of the system.

II. THEORY

We first describe the calculation used to model the echo signal presented in Refs. [10,14–16] and then consider the effects of SE and spatial profile.

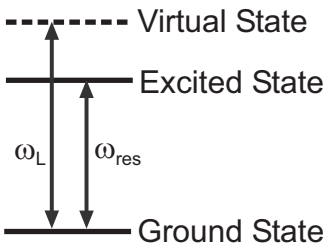

FIG. 3. The AI involves off-resonant standing wave excitation and manipulation of atoms in the ground state. Here, ω_{res} is the atomic resonance frequency and ω_L is the laser frequency.

The system is modeled semiclassically as a collection of two-level atoms. For off-resonant excitation pulses shown in Fig. 3 the excited state can be adiabatically eliminated. During the first standing wave excitation pulse which is applied at $t=0$ the Hamiltonian of the atom-field system is given by

$$H = \frac{\hat{\mathbf{p}}^2}{2M} - \begin{bmatrix} \hbar(\Delta + i\Gamma) & V(\mathbf{r}) \\ V(\mathbf{r}) & 0 \end{bmatrix}. \tag{1}$$

Here $\mathbf{p}$ is the momentum associated with the atom, $\Delta \equiv \omega_L - \omega_{res}$ is the detuning of the laser from the excited state, Γ is the effective radiative decay rate of the excited state, and $V(\mathbf{r})$ is the spatially periodic atom-field coupling. Because the laser field creates a standing wave, $V(\mathbf{r})$ is given by

$$V(\mathbf{r}) = \frac{\mu E_0}{2} \cos\left(\frac{\mathbf{q}\cdot\mathbf{r}}{2}\right), \tag{2}$$

where E_0 is the amplitude of the electric field, μ is the dipole moment, and $\mathbf{r}$ is the position of the atom in the potential. If the pulses are sufficiently short, the distance the atoms move during the pulse is small compared to the period of the standing wave potential $\lambda/2$. It is then possible to ignore the kinetic energy term $\frac{\hat{\mathbf{p}}^2}{2M}$ in the Hamiltonian (Raman-Nath approximation) during the excitation pulse. Using this approximation, the expression for the interaction potential energy for the ground state becomes

$$U(x) = \frac{V^2(x)}{\hbar(\Delta + i\Gamma)} \simeq \frac{\hbar\omega_1^2}{8(\Delta + i\Gamma)} \cos(qx), \tag{3}$$

where x is the position of the atom along the direction of $\mathbf{q}$, $\omega_1 = \frac{\mu E_0}{\hbar}$ is the Rabi frequency, and a constant term has been ignored.

For an initial atomic plane wave, the wave function is $|\psi(t=0)\rangle \propto e^{ik_0 x}$, where k_0 is the initial momentum. Applying the time evolution operator we obtain

$$|\psi(t)\rangle = \exp\left[-\frac{i}{\hbar}\int_0^t \tilde{H}(t')dt'\right]|\psi(0)\rangle \tag{4}$$

at any time, t, during the excitation pulses. Here $\tilde{H}$ is the effective Hamiltonian. For an excitation pulse of duration $t = \tau_1$ we find

$$|\psi(\tau_1)\rangle = \exp[i\phi_1 \cos(qx) + ik_0 x] \tag{5}$$

where $\phi_1 \equiv -\frac{\omega_1^2}{8(\Delta+i\Gamma)}\tau_1$ is the area of the first standing wave pulse. For the far-detuned case, $\Delta \gg \Gamma$, we can ignore the effect of Γ in Eq. (3) so that $\phi_1 = -\frac{\omega_1^2}{8\Delta}\tau_1$.

Next, the Jacobi-Anger expansion can be used to rewrite $|\psi(\tau_1)\rangle$ after the standing wave interaction so that

$$\psi(\tau_1) = \sum_{n=-\infty}^{\infty} i^n J_n(\phi_1) e^{i(nq+k_0)x}, \tag{6}$$

where $J_n(x)$ is the nth order Bessel function of the first kind. Each Fourier component of index n in the summation represents a process transferring $n\hbar q$ momentum to the atom. Each two-photon process involves absorption of a photon from one traveling wave component of the standing wave pulse and stimulated emission in the direction of the other traveling wave. Therefore, the Fourier series represents a superposition of plane waves separated in momentum by $\hbar q$ with amplitudes weighted by Bessel functions. Equation (6) can be expanded to give

$$\begin{aligned}|\psi(\tau_1)\rangle = {} & J_0(\phi_1)|p_0\rangle + iJ_1(\phi_1)|p_0+\hbar q\rangle + iJ_1(\phi_1)|p_0-\hbar q\rangle \\ & - J_2(\phi_1)|p_0+2\hbar q\rangle - J_2(\phi_1)|p_0-2\hbar q\rangle + \cdots,\end{aligned} \tag{7}$$

where $|p_0\rangle \equiv e^{ik_0 x}$ and $|p_0+n\hbar q\rangle \equiv e^{i(k_0+nq)x}$.

After the standing wave pulse is turned off, the state will undergo free space evolution according to

$$H = \frac{p^2}{2M} = \frac{\hbar^2(nq+k_0)^2}{2M}. \tag{8}$$

The atomic density distribution after the first pulse can then be calculated as

$$\begin{aligned}\psi^*\psi = {} & \sum_{n,n'} i^{(n-n')} J_n(\phi_1) J_{n'}(\phi_1) \\ & \times e^{i[(n-n')qx-(n^2-n'^2)\omega_q t]} e^{-2i(n-n')\sqrt{\omega_0'\omega_q}t}.\end{aligned} \tag{9}$$

To detect the density modulation present in the ground state after the first standing wave pulse, a traveling wave readout pulse must be applied. The readout pulse is at the same frequency as the excitation pulse and is applied along $\mathbf{k}_2$. Light is backscattered off the atomic density grating along $\mathbf{k}_1$. This detection scheme ensures that only momentum states differing by $q=2k$ will contribute to the signal. The signal is proportional to the amplitude of the spatial harmonic with period $\lambda/2$. In our case, the spatial harmonics are restricted to $n-n' \equiv -\eta = \pm 1$. Thus, with a change of summation indices, we can simplify Eq. (9) to obtain

$$\begin{aligned}\psi^*\psi = {} & \sum_{\eta=\pm 1} i^{-\eta} \sum_n J_n(\phi_1) J_{n+\eta}(\phi_1) \\ & \times e^{i[-\eta qx+\eta(2n+\eta)\omega_q t]} e^{2i\eta\sqrt{\omega_0'\omega_q}t}.\end{aligned} \tag{10}$$

It is possible to compress the sum over n in Eq. (10) by using a Bessel function identity given in Ref. [17].

$$i^\nu J_\nu(2u' \sin(\alpha/2)) = \sum_{l=-\infty}^{\infty} e^{i\nu\alpha/2} J_{l+\nu}(u') J_l(u') e^{il\alpha} \tag{11}$$

so that

$$\psi^*\psi = 2J_1(2\phi_1 \sin(\omega_q t))\cos(qx - 2\sqrt{\omega_0'\omega_q}t). \tag{12}$$

this is the signal that is relevant to Kapitza-Dirac scattering for neutral atoms which was demonstrated in Ref. [18]. The term containing ω_0' in the above equation is due to the initial velocity of the atoms. The recoil period can be extracted by measuring the amplitude of the density grating as a function of t. However, Eq. (12) must be integrated over the velocity distribution. The distribution would cause the atoms to dephase on a time scale much smaller than ω_q^{-1} unless the sample temperature is ultracold as in a Bose-Einstein condensate (BEC) [19]. However, if a second pulse is applied at $t=T$ the effect of Doppler dephasing can be canceled and an echo signal can be observed at $t=2T$. Even if the sample is not ultracold, it is possible to observe the effects of recoil by measuring the echo amplitude as a function of T. We note that for our experimental conditions, the most probable speed associated with the atom cloud $v_T \sim 20 v_r$ where $v_r = \hbar q/M$ is the recoil velocity.

After the first standing wave pulse, the system undergoes free space evolution according to Eq. (8). The second standing wave excitation pulse (pulse area ϕ_2) affects the atomic plane waves in the same way as the first excitation pulse affects the initial plane wave so that

$$\begin{aligned}\psi(t=T) = {} & \sum_{n,m} i^{(n+m)} J_n(\phi_1) J_m(\phi_2) \\ & \times e^{i[(m+n)qx - n^2\omega_q T - nqv_0 T]} e^{i(k_0 x - \omega_0' T)},\end{aligned} \tag{13}$$

where $v_0 = \hbar k_0/M$ is the initial velocity of the atomic plane wave.

At a time t after the second standing wave pulse, the wave function evolves as

$$\psi(t) = \psi(T) e^{-i[\omega_0' + (m+n)qv_0 + (n+m)^2\omega_q]t}. \tag{14}$$

Using Eq. (14) to find $\psi^*\psi$ it can be shown that

$$\begin{aligned}\psi^*\psi = {} & \sum_{n,m,n',m'} J_n(\phi_1) J_{n'}(\phi_1) J_m(\phi_2) J_{m'}(\phi_2) \\ & \times i^{(n+m-n'-m')} e^{i(m+n-n'-m')qx} \\ & \times e^{-iqv_0[(n+m-n'-m')t + (n-n')T]} \\ & \times e^{-i(n^2-n'^2)\omega_q T} e^{-i[(n+m)^2-(n'+m')^2]\omega_q t}.\end{aligned} \tag{15}$$

The echo technique ensures that only terms independent of the initial velocity contribute to the signal. In addition, only momentum states differing by $\hbar q$ will interfere and result in backscattering from the readout pulse. Using these conditions, it can be shown that

$$\begin{aligned}\psi^*\psi(t=2T) = {} & 2(-1)^N \cos[q(x - v_0\Delta t)] \\ & \times J_N(2\phi_1 \sin(\omega_q \Delta t)) \\ & \times J_{N+1}(2\phi_2 \sin[\omega_q(NT + \Delta t)]),\end{aligned} \tag{16}$$

where $\Delta t = t - 2T$ and $N=1$ for the echo at $t=2T$. Assuming that the time between standing wave pulses is much greater than the dephasing time of the echo ($qv_T T \gg 1$), we can average over the Maxwell-Boltzmann velocity distribution of the sample to obtain

$$\psi^* \psi \propto \exp\left[-\left(\frac{qv_T \Delta t}{2}\right)^2\right] J_1(2\phi_1 \sin(\omega_q \Delta t)) \times J_2(2\phi_2 \sin[\omega_q(T+\Delta t)]). \quad (17)$$

This expression is periodic in Δt and T with a frequency ω_q. The factor containing the first-order Bessel function in Eq. (17) shows that ω_q can be determined by keeping the time between pulses, T, fixed and observing the periodic signal as a function of Δt within the echo envelope if the sample is sufficiently cold. The duration of the echo envelope in the vicinity of $t=2T$ is inversely proportional to the most probable speed of velocity distribution along the direction of the excitation pulses, as shown in Fig. 2. There will only be an echo signal over an interval Δt in which the atoms move a distance of the order of the grating spacing $[\Delta t < (qv_T)^{-1}]$. For the case where $\Delta t \ll 2T$, Eq. (17) can be written in a simpler form by assuming that the interaction pulse areas are small ($\phi_1 \sim \phi_2 \sim 1$) [10] so that

$$\psi^* \psi \sim (\omega_q \Delta t) \exp\left[-\left(\frac{qv_T \Delta t}{2}\right)^2\right] J_2(2\phi_2 \sin(\omega_q T)). \quad (18)$$

For a laser cooled sample with a temperature of $\sim 50\ \mu$K, ω_q can be measured precisely by measuring the echo amplitude as a function of the time between excitation pulses, T. The detection techniques used in the measurements are either sensitive to the electric field amplitude of the backscattered light or the associated intensity. For the case of electric field detection, the echo envelope is shown in Fig. 2. For both electric field detection and intensity detection, the echo envelope is recorded with a detection system with a suitably high bandwidth.

To obtain the echo amplitude we integrate the square of the echo envelope over Δt for a fixed value of T. The echo envelope is integrated over the duration of the signal (several μs). For electric field detection, we take the positive square root of the integrated signal to obtain the echo amplitude. For intensity detection, the integrated signal represents the echo amplitude. To study the T-dependent behavior of the signal, we fit the echo amplitude to $\psi^* \psi$ for electric field detection and $|\psi^* \psi|^2$ for intensity detection. We therefore use the term echo amplitude throughout the paper to describe the strength of the T-dependent signal obtained from either of these techniques.

We now describe several aspects of the signal shape following a more detailed derivation that includes the effects of SE and spatial profile of the excitation beams.

A. Spontaneous emission

The derivation presented here is based on Refs. [14,15,20]. Equation (18) neglects several factors that affect the signal shape such as SE and it is inadequate for fitting the echo amplitude to obtain a precision measurement of ω_q. Equation (18) was derived as the expression for the echo signal for the case $\Delta \gg \Gamma$. Therefore the effect of spontaneous emission is ignored in Eq. (3). In general, the potential energy is complex and the pulse area is given by

$$\phi_1 = \frac{-\omega_1^2 \tau}{8(\Delta + i\Gamma)} = u(\tau) e^{i\theta} \quad (19)$$

where

$$u(\tau) = \frac{-\omega_1^2 \tau}{8\sqrt{\Delta^2 + \Gamma^2}} \quad (20)$$

and

$$\theta = \tan^{-1}\left(-\frac{\Gamma}{\Delta}\right). \quad (21)$$

The definition of ϕ_1 in Eq. (19) is consistent with the definition of ϕ_1 following Eq. (5). We note that θ has a similar form to the phase shift in the emitted radiation due to the damping force for the case of a driven-damped harmonic oscillator. The effect of θ is to cause a delay in the formation of the grating. As shown in this treatment, θ influences the shape of the echo envelope and the T-dependent echo amplitude. Using Eqs. (19)–(21) we can modify the expression for atomic density $\psi^* \psi$ following the same steps outlined in the preceding section based on Refs. [14,15,20]. Defining $\eta = n + m - n' - m'$ we obtain

$$\psi^* \psi = \sum_{m,n,\eta} i^{\eta} J_n(u(\tau_1) e^{i\theta}) J_{n+\eta N}(u(\tau_1) e^{-i\theta}) J_m(u(\tau_2) e^{i\theta}) J_{m-\eta(N+1)}(u(\tau_2) e^{-i\theta}) e^{i\eta q x} e^{i\eta N(2n+\eta N)\omega_q T} e^{-i\eta q v_0 \Delta t} e^{-i\eta[2(n+m)-\eta]\omega_q T}. \quad (22)$$

Here, τ_2 represents the duration of the second standing wave pulse. In order to simplify Eq. (22) we need an identity similar to Eq. (11) that allows complex arguments. The Appendix describes the steps required to derive this identity which is contained in Eq. (A13). Using Eq. (A13), we obtain an expression for the atomic density in the vicinity of $t=2T$ which is given by

$$\psi^* \psi = \sum_{\eta=-\infty}^{\infty} e^{i\eta q x} e^{-i\eta q v_0 \Delta t} \left(\frac{\sin(\eta\omega_q \Delta t + \theta)}{\sin(\eta\omega_q \Delta t - \theta)}\right)^{\eta N/2} \left(\frac{\sin[\eta\omega_q(NT + \Delta t) + \theta]}{\sin[\eta\omega_q(NT + \Delta t) - \theta]}\right)^{-\eta(N+1)/2} \times J_{\eta N}(2u(\tau_1)\sqrt{\sin(\eta\omega_q \Delta t - \theta)\sin(\eta\omega_q \Delta t + \theta)}) J_{-\eta(N+1)}(2u(\tau_2)\sqrt{\sin[\eta\omega_q(NT + \Delta t) - \theta]\sin[\eta\omega_q(NT + \Delta t) + \theta]}). \quad (23)$$

Because our detection scheme is only sensitive to interference by momentum states that differ by $\hbar q$ ($\eta = \pm 1$) and we observe

the $\lambda/2$ spatial harmonic at $t=2T$ $(N=1)$, the infinite sum is truncated and Eq. (23) can be written as

$$\psi^*\psi = \cos[q(x-v_0\Delta t)]\left(\frac{\sin(\omega_q\Delta t+\theta)}{\sin(\omega_q\Delta t-\theta)}\right)^{1/2}\left(\frac{\sin[\omega_q(T+\Delta t)-\theta]}{\sin[\omega_q(T+\Delta t)+\theta]}\right)$$
$$\times J_1(2u(\tau_1)\sqrt{\sin(\omega_q\Delta t+\theta)\sin(\omega_q\Delta t-\theta)})J_2(2u(\tau_2)\sqrt{\sin[\omega_q(T+\Delta t)+\theta]\sin[\omega_q(T+\Delta t)-\theta]}). \quad (24)$$

Integrating this expression over the Maxwell-Boltzmann distribution to account for all velocity classes it can be shown that

$$\psi^*\psi_{\text{total}} \propto \exp\left[-\left(\frac{qv_T\Delta t}{2}\right)^2\right]\left(\frac{\sin(\omega_q\Delta t+\theta)}{\sin(\omega_q\Delta t-\theta)}\right)^{1/2}\left(\frac{\sin[\omega_q(T+\Delta t)-\theta]}{\sin[\omega_q(T+\Delta t)+\theta]}\right)$$
$$\times J_1(2u(\tau_1)\sqrt{\sin(\omega_q\Delta t+\theta)\sin(\omega_q\Delta t-\theta)})J_2(2u(\tau_2)\sqrt{\sin[\omega_q(T+\Delta t)+\theta]\sin[\omega_q(T+\Delta t)-\theta]}). \quad (25)$$

This expression is equivalent to Eq. (17) for the case where $\Gamma\to 0$. We will now discuss some qualitative differences between the predictions of Eqs. (17) and (25). We will separate the discussions into a description of the echo envelope and a description of the T-dependent signal that has a period T_{recoil}. Equation (18) predicts a symmetric echo envelope if $\Delta t \ll T_{\text{recoil}}$ and $\phi_1 \sim \phi_2 \sim 1$. For large interaction pulse areas or ultracold samples Eq. (17) rather than Eq. (18) is valid and predicts an asymmetric echo envelope. The solid curve in Fig. 4 shows the symmetric echo envelope predicted by Eq. (17) if $\Delta \gg \omega_1$. When the first standing wave pulse area increases, the echo envelope remains symmetric but becomes narrower. This is presumably due to the broadening of the velocity distribution of the atoms caused by the standing wave interaction. As the second pulse area increases, the relative amplitude of the first lobe of the echo envelope becomes larger and the amplitudes of the two lobes show a cyclical dependence on pulse area. A representation of an asymmetric shape due to a change in pulse area is shown in Fig. 4 as a dotted line. Equation (17) also shows that the relative amplitudes of the lobes will change in a more complicated cyclical manner if the time between pulses, T, is varied. With pulse area and pulse separation fixed, Eq. (25) predicts that the echo envelope will have an asymmetric shape due to SE, as shown by the dashed line in Fig. 4. Other factors affecting the echo envelope include effects such as gravity that affect both arms of the interferometer are discussed in Ref. [12]. SE also has the effect of delaying the time at which the signal zero occurs in the vicinity of $t=2T$.

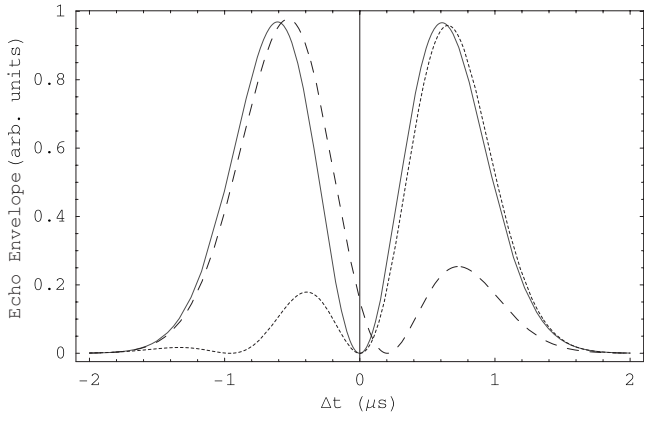

FIG. 4. Echo envelope: Solid curve shows echo envelope predicted by Eq. (17) for $T=1$ ms, $\phi_1=2.5$, and $\phi_2=2.6$. The dotted line shows an asymmetric shape due to the variation in pulse area for $T=1$ ms, $\phi_1=2.5$, and $\phi_2=5$. The dashed line shows an asymmetric shape due to SE modeled by Eq. (25) for $T=1$ ms, $u_1=2.5$, $u_2=2.6$, and $\theta=-0.02$. The dashed line also shows a delay in the position of the signal zero in the vicinity of $\Delta t=0$. All curves are calculated using a temperature of 100 μK and assuming that the atomic species is ^{85}Rb.

A comparison of the echo amplitude predicted by Eqs. (18) and (25) is shown in Fig. 5. In the presence of SE the signal amplitude is predicted to have a pronounced asymmetry with respect to the zeros of the function. The zeros separated by T_{recoil} are shown in Fig. 5. This can attributed to the nonsinusoidal nature of the interaction potential described by Eq. (3). To extract a precision measurement of ω_q it is crucial to fit the data using an expression that accounts for these asymmetric features [which are modeled by Eq. (25)]. This equation also predicts a negative temporal offset in the echo amplitude due to SE. The temporal offset can be ~ 1 μs for typical experimental conditions. Therefore, the delay in the

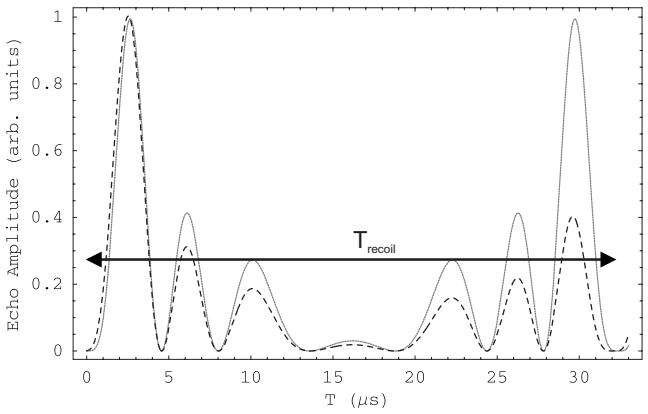

FIG. 5. Echo amplitude vs T with and without spontaneous emission: Solid line shows echo amplitude vs T based on Eq. (18) where $\omega_q=97\,000$ s^{-1}, and $\phi_2=6$. The dashed line shows the echo amplitude vs T for Eq. (25) where $\omega_q=97\,000$ s^{-1}, $u_2=6$, and $\theta=-0.03$. The dashed line shows an asymmetry in the periodic signal in the presence of SE, as well as a temporal shift.

formation of the grating due to SE effectively decreases the values of T at which the zeros occur. Although this effect does not change the period of the signal, ω_q is typically measured by fitting to two widely separated periods [11]. If the expanding atomic cloud samples different parts of the standing wave potential or if Δ varies (due to the Doppler shifts associated with the falling atomic cloud) when T is varied, θ will vary for the widely separate periods resulting in a systematic effect on the measurement of ω_q. Both the asymmetry and the temporal offset are shown in Fig. 5.

B. Spatial profile

The expression given in Eq. (25) has to be further modified to account for the spatial profile of the interferometry beams. The derivation leading to Eq. (25) assumed that the electric field was a plane wave with uniform amplitude. Due to the Gaussian profile of the AI beams, atoms experience a spatially varying Rabi frequency and, consequently, sample different pulse areas. Equation (25) predicts that increasing the pulse area results in multiple minima per recoil period and the echo amplitude varies more rapidly in the vicinity of the zero. This can be attributed to the interference of higher-order momentum states produced by the first standing wave pulse. However, the signal shape between adjacent zeros is observed to be smoothed out. This effect is attributed to the spatial profile.

The signal shape can be modeled by integrating the Bessel functions in Eq. (25) over a range of Rabi frequencies. This integral results in a generalized hypergeometric function. Although this model resulted in signal shapes that are qualitatively in agreement with the observed signal, we find that the hypergeometric function is not suitable as a fit function. However, the signal shape could be fit more accurately using the function

$$S(T) = AJ_2[b(1 - e^{d\sqrt{\sin(\omega_q T-\theta)\sin(\omega_q T+\theta)}})]\left|\frac{\sin(\omega_q T-\theta)}{\sin(\omega_q T+\theta)}\right|, \tag{26}$$

where A is an overall scale factor and the parameters b and d are related to the pulse area.

Simulations of the signal shape using Eq. (26) show that additional zero crossings are averaged out to give a periodic signal that has only one local minimum per recoil period as shown in Fig. 6. This figure shows that the solid line based on Eq. (26) represents the effect of averaging the echo amplitude over a range of pulse areas.

III. EXPERIMENT

The light used for trapping and interferometry is derived from a single Ti:Sapphire ring laser with an output power of ~1 W. The repump laser is derived from a grating stabilized diode laser. A small portion of the Ti:Sapphire laser light is sent through a saturation absorption spectrometer that includes a dual pass acousto-optic modulator (AOM) operating at ~70 MHz and serving as a tuning element. The laser is locked to the $5S_{1/2}$ $F=3$ to $5P_{3/2}$ $F=4$ trapping transition in ^{85}Rb so that the laser beam used in the experiment is

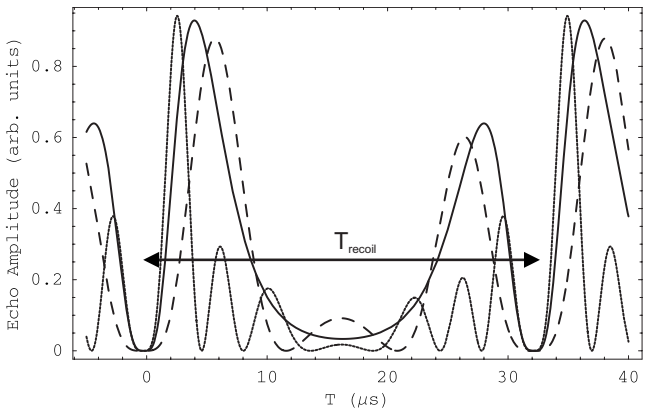

FIG. 6. Echo amplitude vs T showing the effect of spatial profile: The dotted and dashed lines show the echo amplitude vs T given by Eq. (25) with $u_2=6$ and $u_2=2.85$, respectively. The solid curve shows the echo amplitude vs T given by Eq. (26). It can be seen that an average of signals with a range of pulse areas will result in a signal shape that can be described by Eq. (26).

~140 MHz above resonance. A dual-pass AOM (AOM1) is used to frequency shift and amplitude modulate the trapping laser beams. The undiffracted laser beam from AOM1 is sent into another dual-pass AOM (AOM2) operating at ~80 MHz to derive a laser beam at ~300 MHz above resonance. This beam is split and sent through two AOMS (AOM3 and AOM4) operating at ~250 MHz to derive excitation pulses used for atom interferometry that are 50–100 MHz above resonance. We load approximately 10^8 atoms in a magneto-optical trap (MOT) on a time scale of ~100 ms using AOM1 to tune the trapping beams to ~$2\Gamma_N$ below resonance, where $\Gamma_N=(2\pi\tau)^{-1}=6.07$ MHz is the natural linewidth, and the radiative decay time, $\tau=26.20$ ns [21,22]. After turning off the gradient coils in ~500 μs, AOM1 is used to shift the trapping beams to ~$5\Gamma_N$ below resonance and cool the atoms in a molasses for ~5 ms. The trapping beams are then turned off for ~25 ms during which time AOM2, AOM3, and AOM4 are turned on to generate traveling wave components of the standing wave pulses as well as the traveling wave readout pulse. The excitation pulses have approximately the same diameter as the initial size of the cloud (~4 mm). The temperature of the sample is inferred by photographing the ballistic expansion of the cloud using a charge-coupled device (CCD) camera and is typically ~50 μK [23]. The echo signal is detected by backscattering the readout pulse from the sample. In this work, we have used two separate techniques represented in Fig. 7 to detect the echo. Heterodyne detection shown in Fig. 7(a) requires an optical local oscillator (LO) which is derived by using the undiffracted beam from AOM3. The LO is spatially separated from the diffracted beam by ~2.5 cm to minimize decoherence due to scattered light. Pulsing AOM2 ensures that the LO is turned on only for the duration of the excitation and readout pulses, thereby minimizing decoherence due to background light. Pulsing this AOM also ensures that standing wave pulses have an on and/or off contrast of greater than 10^6:1. The backscattered signal is combined with the LO on a balanced heterodyne detector that detects the presence of the echo in

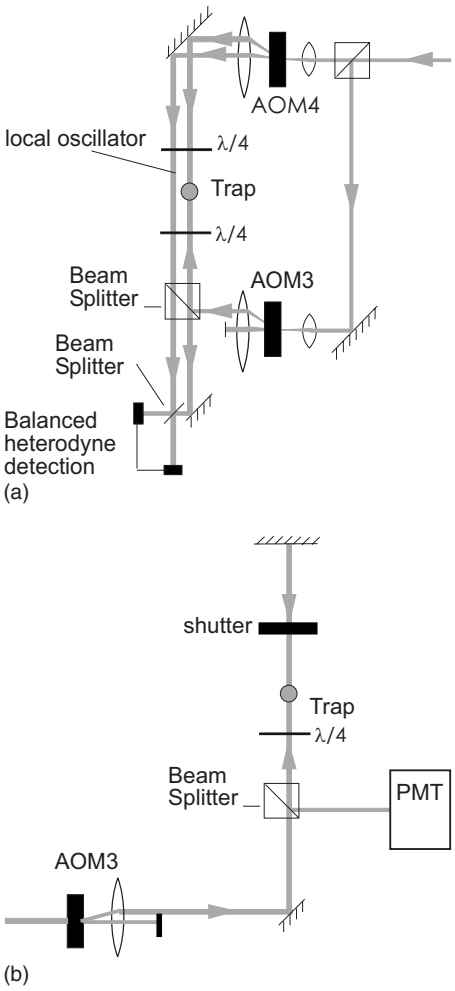

FIG. 7. Experimental setup for the cases of heterodyne detection in (a) and photomultiplier tube (PMT) detection in (b).

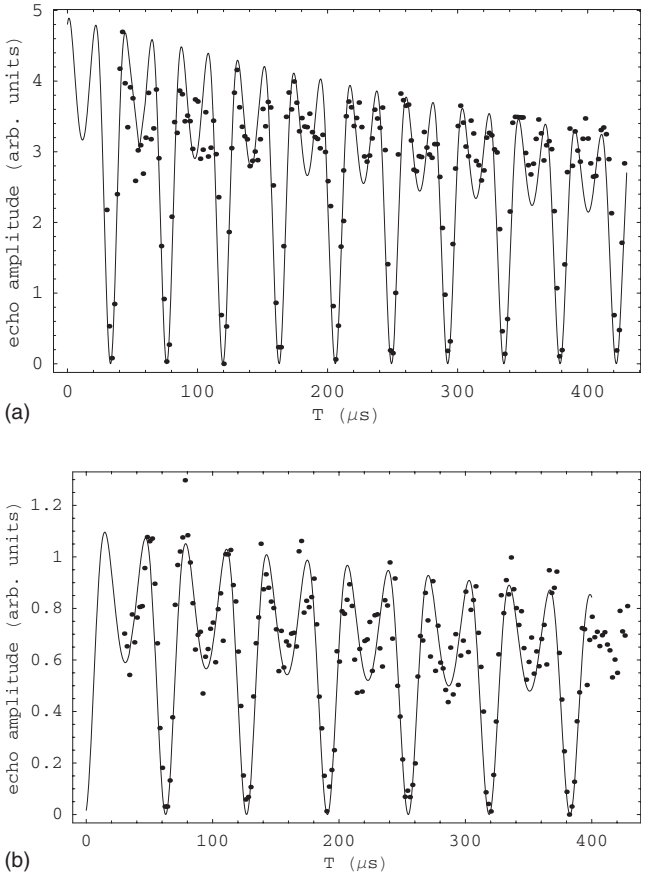

FIG. 8. Echo amplitude vs T: Illustrates the difference in ω_q between (a) counterpropagating excitation beams ($\gamma < 1$ mrad) and (b) excitation beams at an angle of $\gamma = \pi/2$. The data are fit by Eq. (18). The fits give $\omega_q = 9.7 \times 10^4$ s^{-1} and $\phi_2 = 2.1$ for (a) and $\omega_q = 4.9 \times 10^4$ s^{-1} and $\phi_2 = 2.2$ for (b). The uncertainty in ω_q extracted from the fits is $\sim 1/10^3$ and the signal decay time is much smaller than the transit time due to collisions, scattered light, and magnetic field gradients.

the form of a beat note at 250 MHz. The two outputs of the detector are mixed down to dc using the rf oscillator used to drive AOM3 and AOM4. The rf used to produce one of the dc components is phase shifted by $\pi/2$ with respect to the rf used to derive the other dc component. The two dc components are filtered using a 20 MHz low-pass filter and represent the in-phase and quadrature components of the backscattered electric field. This backscattered electric field is the characteristic echo envelope shown in Fig. 2. These signals are squared and integrated over the duration of the signal (a few μs). The positive square root of the sum of the squared signals represents the echo amplitude. AOM2, AOM3, and AOM4 are controlled by digital delay generators. The time base of these generators is referenced to a 10 MHz signal from a Rb atomic clock with an Allan variance of 2×10^{-12} at 100 seconds. The 250 MHz oscillator used to drive AOM3 and AOM4 is also phase locked to the Rb clock.

An alternate detection scheme for intensity detection is shown in Fig. 7(b). This scheme uses only AOM2 and AOM3 as well as a retroreflecting mirror to produce standing wave pulses. A shutter with a closing time of ~ 600 μs for the 4 mm excitation beams is used to block the retroreflection at the time of the readout pulse. In this case, the echo envelope is detected using a gated photomultiplier tube (PMT). The PMT has a rise time of ~ 10 ns and the gate can be fully opened on a time scale of 100 ns. Since the shutter has a jitter of ~ 200 μs, the smallest pulse separations, T, for which the echo can be recorded is ~ 1 ms. The echo envelope, which resembles the square of the signal shape shown in Fig. 2 is recorded using a 20 MHz low-pass filter. The echo envelope is integrated over the duration of the signal (few μs) to obtain the echo amplitude.

The peak intensities of the standing wave beams are $I \sim 10 I_{sat}$ where $I_{sat} = 7.56$ mW cm^2 is the saturation intensity for equally populated magnetic sublevels of the $F = 3$ ^{85}Rb ground state. The durations of the first and second standing wave pulses are 500–800 ns and 30–200 ns, respectively. The echo signal is detected using a readout pulse that has the same detuning as the excitation pulses.

IV. RESULTS

The simplified expression for the echo amplitude in the absence of SE given by Eq. (18) shows that the period of the

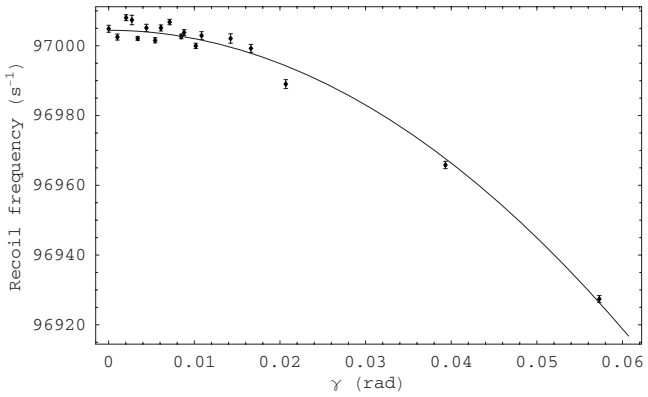

FIG. 9. Shows a fit by data measuring ω_q as a function of γ. The fit function is $b\cos^2(a\gamma/2)$ where $a=0.991\pm0.016$ and $b=97004.4\pm0.6$ s^{-1}.

signal depends on **q**. We have varied **q** by changing the angle β between the traveling wave components of the excitation pulses. When β is set to 180° we observe the periodic signal shown in Fig. 8(a). When $\beta=90°$ the period of the signal is doubled, as expected, as shown in Fig. 8(b). In both cases, the fit by the data was based on Eq. (18) and the point spacing is adequate to resolve the difference in the period. The fits also included a phenomenological decay term to account for the exponential decay of the signal amplitude. The decay in Fig. 8 was primarily due to background light and collisions with rubidium atoms at room temperature. For precise measurements of ω_r we rely on Eq. (26), which includes the effects of both SE and spatial profile, and we take data with a point spacing of ~250 ns. Figure 9 shows the dependence of ω_r on β for the case when the angle is varied over a small range with respect to $\beta=180°$. Both Figs. 8 and 9 show that the recoil frequency has the predicted dependence on angle given by $\omega_q=\hbar q^2/2M$ and $q=2k\sin\beta/2$. For precision measurements of ω_r [11], which are carried out at $\beta\sim180°$, the data are corrected for the angle using the fit shown in Fig. 9, which is based on the predicted expression $\omega_r(\gamma)=\omega_r(180°)\cos^2(\gamma/2)$, where $\gamma=180°-\beta$.

Figure 10 shows a test of the predictions of Eqs. (17) and (25) for the echo envelope. For large detunings the data are accurately modeled by Eq. (17) and symmetric envelopes are obtained. The pulse area is varied by increasing the duration of the second standing wave pulse and the effect of spontaneous emission is varied by changing the detuning. Both effects cause asymmetric signal shapes. Data represented by squares are fit using Eq. (17) and the data represented by circles and triangles are fit using Eq. (25).

We now use the theoretical treatment in Sec. II to illustrate the effects of SE and spatial profile on the echo amplitude. In Fig. 11 the data represent a single recoil period. The point separation is 250 ns and fits are based on Eqs. (18), (25), and (26). It is clear that the expression based on Eq. (26) that includes the effects of both SE and spatial profile is necessary for obtaining an accurate fit to the amplitude of the periodic signal.

To illustrate the importance of Eq. (26) for a precision measurement, we show a typical measurement of ω_q in Fig. 12. The echo amplitude is recorded over two widely separated periods. In this case a multiparameter fit based on Eq. (26) gives a fit error for ω_q of ~3 parts per 10^6 (ppm). The fit also includes a Gaussian decay parameter to account for the signal decay. The other fit parameters (A,b,d,θ) are determined to a precision of ~10%. Similar fit errors for A, b, d, and θ are obtained for all fits based on Eq. (26) (Figs. 11–13 and 15). With the exception of Fig. 12 (in which the fit

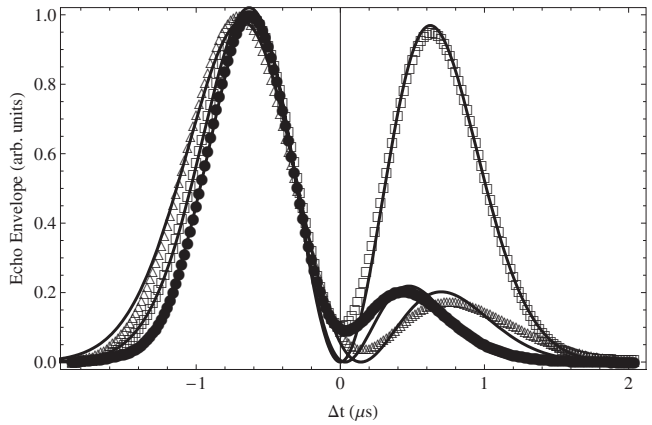

FIG. 10. Background subtracted traces of the echo envelope obtained by backscattering the readout pulse from the atomic cloud. The traces represent an average of 32 repetitions. The typical background is typically 1% of the amplitude of the echo envelope. Squares represent a symmetric echo envelope recorded with $\Delta=55$ MHz and $\tau_2=155$ ns. Fit to Eq. (17) (solid line) gives a temperature of ~80 μK, $\phi_1=1.4$, and $\phi_2=2.8$. Circles represent asymmetric echo envelope obtained by increasing the second pulse duration to $\tau_2=300$ ns. Fit to Eq. (25) (solid line) gives temperature of 90 μK, $u_1=0.9$, and $\theta=-.025$. Triangles represent asymmetric echo envelope obtained with $\Delta=25$ MHz and $\tau_2=155$ ns. Fit to Eq. (25) (solid line) gives temperature of 60 μK, $u_1=4$, and $\theta=-0.03$. The central minima at $\Delta t=0$ is nonzero due to a limitation of the PMT detection system. The signal levels at $\Delta t=\pm2$ μs represent the true zero of the signal. For heterodyne detection, (see data overlaid in Fig. 2) the signal at $\Delta t=0$ has been verified to be zero within experimental error.

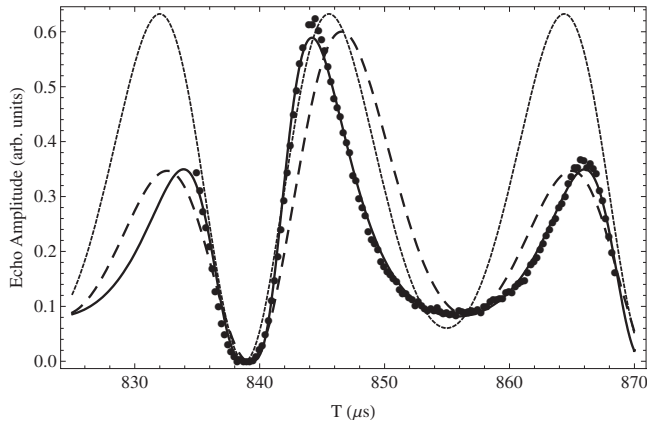

FIG. 11. Echo amplitude vs T. The data for $\Delta=50$ MHz (solid circles) are fit with Eq. (18) (dotted line), Eq. (25) (dashed line), and Eq. (26) (solid line).

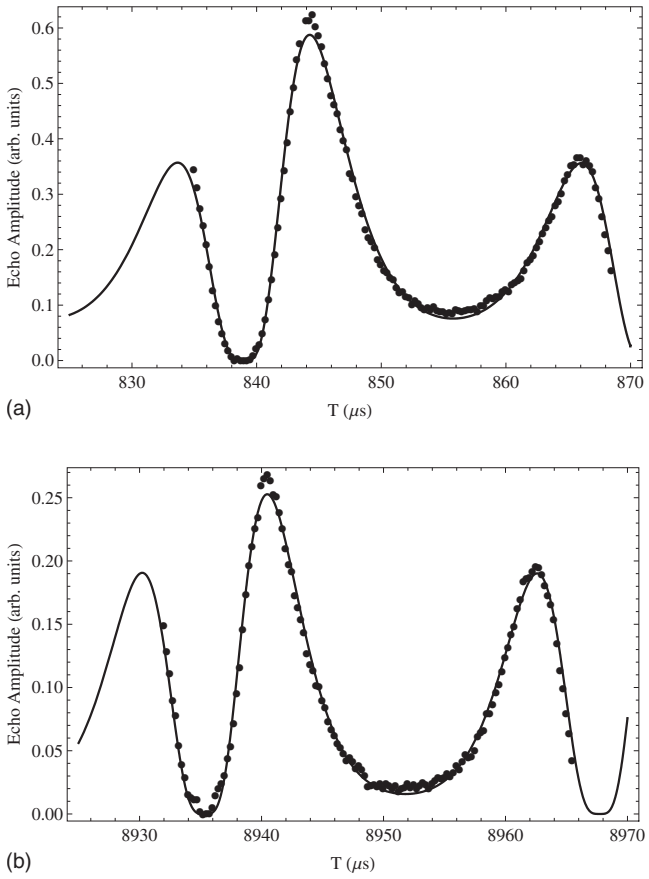

FIG. 12. A typical recoil measurement with $\Delta=50$ MHz. The measurement is carried out by fitting the data by Eq. (26) and consists of one recoil period recorded at $T\sim900$ μs and a second recoil period recorded at $T\sim9000$ μs. The fit gives $\omega_q=97\,008.5(4)$ s^{-1}.

error for ω_q is ~3 ppm), the fit error for ω_q is typically $\sim1/10^3$. The data in Fig. 12 have a long decay time compared to the time scale in Figs. 8 because the effects of background collisions, stray light, and magnetic field gradients have been reduced. The importance of including the effects of SE and spatial profile on a precision measurement of ω_q are quite dramatic. For example, ω_q can be determined to a precision of $\sim1/1000$ if the signal decay time is ~1 ms [10,13]. Although the signal decay time in Fig. 12 has been increased by only a factor of ~20 the precision in ω_q has improved by a factor of ~1000. Since the precision increases linearly with T, it can be seen that the improvements to the theoretical expressions used in the fits have contributed as much as a factor of ~50 to the improvement in precision.

To understand the predictions for the effect of the atom-field coupling on the echo amplitude, we vary the pulse area ϕ_2 by adjusting the duration of the second standing wave pulse as shown in Fig. 13. The data were fit using expression (26). As expected, the signal shape shows a sinusoidal dependence for small pulse durations (~40 ns) and sharply defined minima for longer pulse durations (~500 ns). The narrowing of the signal shape in the vicinity of the zeroes is attributed to interference of higher-order momentum components that are rephased by the second standing wave pulse. Thus, controlling the pulse width plays an important role in

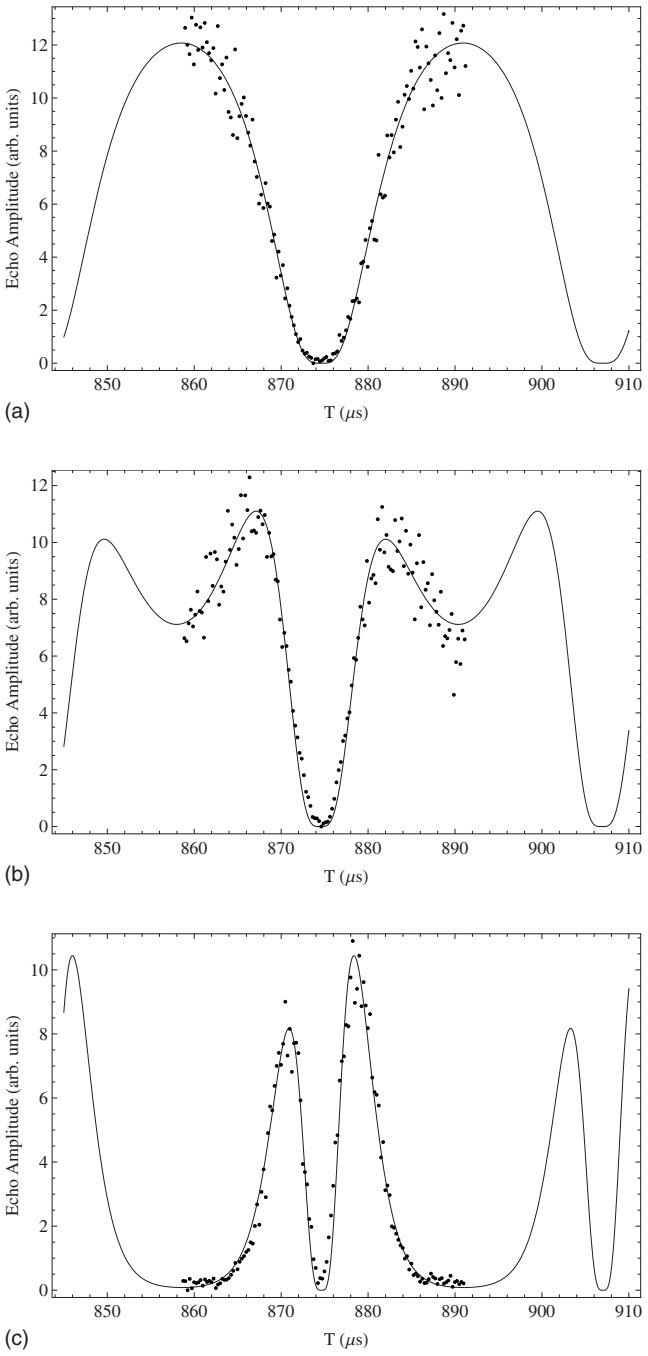

FIG. 13. The effect of varying the pulse area of the second excitation pulse on the signal shape with $\Delta=70$ MHz. The fit functions are based on Eq. (26) and the pulse durations are (a) 40 ns, (b) 60 ns, and (c) 100 ns.

decreasing the relative uncertainty in determining the positions of the zeros.

Figure 14 shows the dependence of the effective pulse area [given by the product of the fit parameters b and d in Eq. (26)] on τ_2. For these data the Raman-Nath criterion was satisfied for pulse widths up to ~3 μs. We note that in Eq. (18) the pulse area of the second standing wave pulse is defined as $\phi_2=(\omega_1^2/8\Delta)\tau_2$ where τ_2 is the pulse duration. This equation predicts that the pulse area should increase

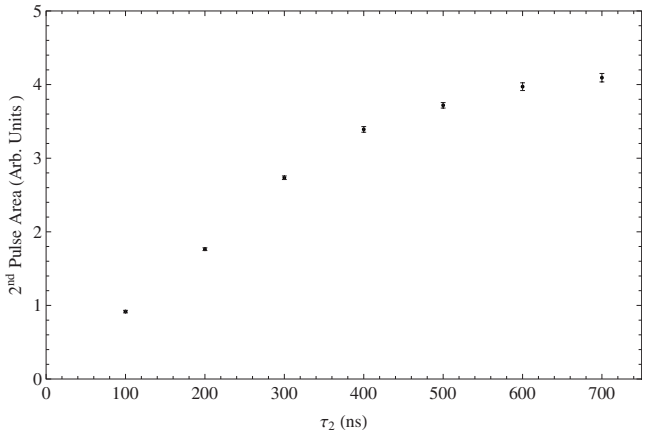

FIG. 14. The measured pulse area as a function of second excitation pulse duration.

linearly with pulse duration. Therefore the slope of pulse area vs τ_2 represents the strength of the atom-field interaction. However, Fig. 14 shows that the effective pulse area increases linearly for small τ_2 and remains unchanged for larger τ_2. We explain this effect by noting that the bandwidth of the first pulse limits the number of momentum states diffracted at $t=0$. As τ_2 increases, the pulse area extracted from the fits increases as more high-order momentum states are rephased. When the second pulse is comparable in duration to the first excitation pulse, all higher-order momentum states excited by the first pulse can be rephased. Therefore, there is no change in the pulse area extracted from the fits if the second pulse duration is further increased. We note that the bandwidth of the second standing wave pulse decreases with increasing pulse duration. Although this reduces the order of recoil components that are rephased, it would also lead to a decrease in measured pulse area which is not observed. The measured beam power, spatial profile, and pulse duration can also be used to infer the pulse area. The value of the pulse area extracted from fit parameters b and d agrees with the experimental value within a factor of 2 for pulse durations up to ~400 ns in Fig. 14.

To test the effects of SE on the echo amplitude, we varied the parameter θ given in Eq. (21) by changing the detuning of the standing wave pulses. It can be seen from Fig. 15 that SE produces a pronounced asymmetry in the echo amplitude in the vicinity of the zeros that is predicted by theory. The data is once again fit to Eq. (26).

Figure 16 shows the associated effect of SE on the temporal offset of the T dependent signal. Here θ is varied by changing either the Δ or τ_2. It is clear on the basis of Eq. (21) that θ should depend on Δ. As discussed later in this section, θ is also influenced by τ_2. In Fig. 16 the temporal offset is extracted from a fit to a single recoil period in the vicinity of ~1 ms based on Eq. (26). Independent measurements in Ref. [11] have shown that the temporal offset does not affect the recoil frequency. However, in the presence of cloud launch, as T is varied, the detunings for the two excitation pulses are not the same. In addition, some atoms only sample a limited extent of the spatial profile. This causes changes in the value of θ extracted from fits taken at different pulse separations,

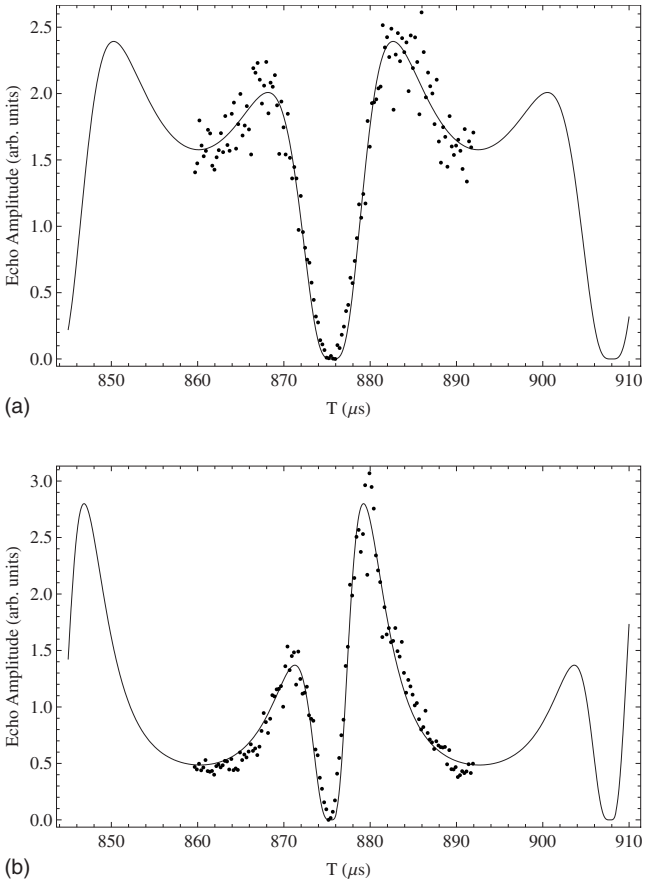

FIG. 15. The effect of varying θ on the signal amplitude. In this case θ was decreased by reducing the detuning and the signal shape is fit to Eq. (26). The values of θ are (a) −0.018 and (b) −0.034.

T. Although this effect is generally small, a systematic variation in the temporal shift implies a variation in the value of ω_q since the function used to fit the data is not periodic in this case. Therefore, high precision studies of ω_q rely on

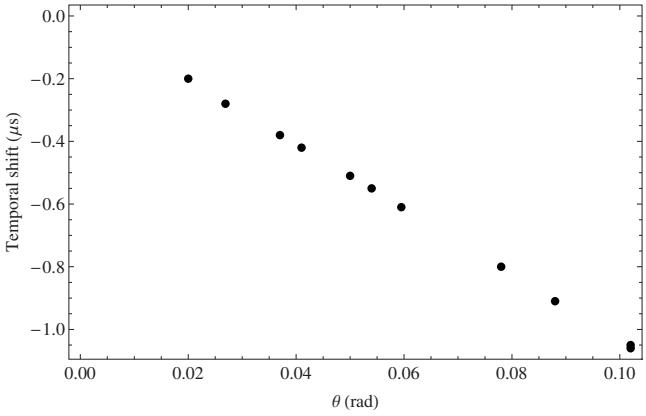

FIG. 16. Temporal shift extracted by fitting to a single recoil period. In this case the temporal shift was varied by changing the Δ and τ_2. The shift is proportional to the measured θ parameter. The error bars on the vertical axis are negligible and the error in the value of θ extracted from the fit is ~5%. The horizontal axis represents the absolute value of θ measured from the fits.

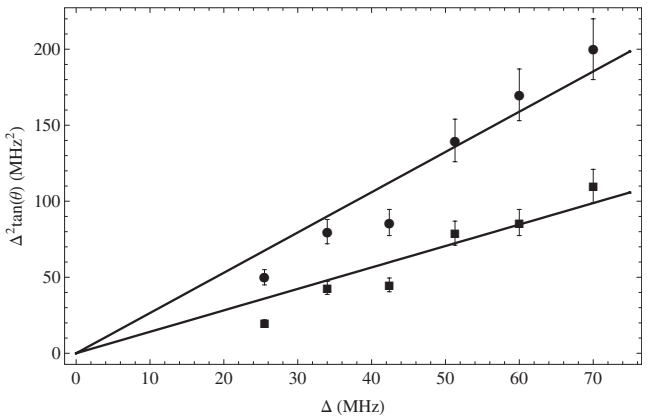

FIG. 17. $\Delta^2 \tan(\theta)$ vs Δ shows a linear dependence. Circles represent $\tau_2=220$ ns and squares represent $\tau_2=120$ ns. The slopes represent the variation in the effective radiative rate of the system and are 2.0 and 3.5 MHz for $\tau_2=120$ ns and $\tau_2=220$ ns, respectively.

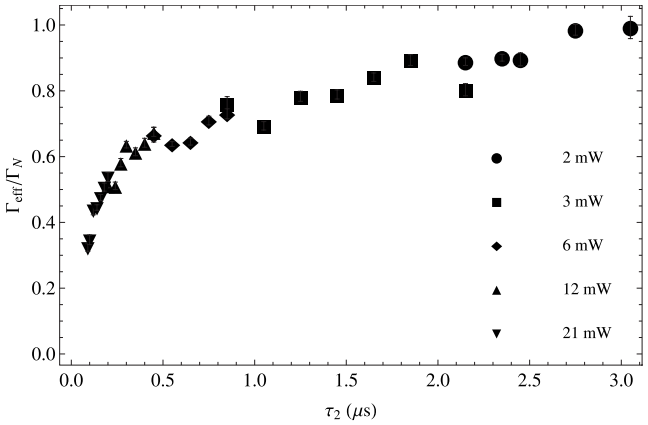

FIG. 18. Measured value of Γ_{eff} vs τ_2. The effective radiative rate is scaled relative to Γ_N. The power of the second standing wave pulse was adjusted to ensure sufficient signal to noise. The diameter of the interferometry beam was approximately 1 cm, which corresponds to a peak Rabi frequency of $\omega_0 \sim 5\Gamma_N$ and $\Delta=40$ MHz. The maximum Γ_{eff} observed is $\sim 1\Gamma_N$ within error. The errors in Γ_{eff} extracted from fits were typically the size of the points shown in the graph.

quantifying this effect. The variation in θ between widely separated recoil periods shown in Fig. 12 is negligible at higher detunings ($\sim$500 MHz). Under these conditions, the variation in the temporal offsets predicted by fits to widely separated periods can be as small as 0.01 ns. In comparison, the recoil period is determined to a precision of $\sim$30 ns for a $\sim$3 ppm measurement shown in Fig. 12.

A plot of $\Delta^2 \tan(\theta)$ (using θ extracted from fits and forcing the fits through the origin) shows the linear trend predicted by Eq. (21) as a function of Δ for suitably large detuning as shown in Fig. 17. It can be seen that the slope in Fig. 17 represents the effective radiative rate of the system (rather than the radiative rate associated with an isolated atom). This figure also shows that the effective radiative rate varies as a function of the duration of the second excitation pulse, τ_2. We discuss a possible explanation for this effect based on numerical simulations using a dressed state analysis. An outline of these simulations is discussed at the end of this paper.

To explore the influence of spontaneous emission in more detail, we extract the quantity θ defined by Eq. (21) from the fits. To improve the accuracy of θ extracted from fits, we used data containing two adjacent recoil periods at $T \sim 1$ ms. The dependence of Γ (extracted from θ) on τ_2 for a fixed detuning is shown in Fig. 18. To acquire this data, it was necessary to progressively reduce the intensity of the second standing wave pulse as the pulse duration was increased to ensure a suitable signal to noise ratio. The data show that the effective radiative rate varies smoothly as a function of τ_2 and approaches the expected value for an isolated atom for suitably long pulses. Since the intensity of the second standing wave pulse was varied for the data in Fig. 18, we verified that the measured radiative rate does not show a strong dependence on the intensity of the second standing wave pulse. The continuous variation of Γ_{eff} in Fig. 18 also suggests that any intensity dependence was insignificant.

It is interesting to note that the uncertainty in the asymptotic value of Γ_{eff} is of the order of 1%. If the theoretical basis for the dependence of Γ_{eff} on τ_2 is fully understood, this technique could potentially be exploited for an atom interferometric measurement of the radiative rate. However, such a measurement would be useful only if a precision of $\sim$0.1% (characteristic of the best measurements of radiative rates) can be obtained [22]. The experimental challenges associated with improving this measurement could involve different methods of data analysis. In this work, θ is extracted from fits to one or two adjacent recoil periods. Therefore, a higher precision can be expected by recording a sequence of recoil periods. Alternatively, it may be possible to improve the precision by increasing the accuracy with which the temporal offset can be determined and using the correlation between the temporal offset and θ as shown in Fig. 16 to extract Γ_{eff}. To reduce the error in the temporal offset, it would be necessary to record widely separated zeroes of the echo amplitude and measure ω_q, and then find the temporal offset by extrapolation.

In summary, the effect of spontaneous emission was introduced as a phenomenological decay rate in Eq. (1). The theoretical predictions for SE presented in this paper have been successful at predicting the echo envelope and T-dependent echo amplitude as shown in Figs. 10–13 and 15 and contributed to a considerable improvement in the precision of ω_q. The behavior of the temporal offset in Fig. 16 and the detuning dependence in Fig. 17 are also consistent with predictions. However, the value of θ extracted from the fits shows that the measured radiative rate is not that of an isolated atom and that the radiative rate depends on the pulse duration τ_2 as shown in Figs. 17 and 18.

To model the effect seen in the experiment (Fig. 18) we have carried out numerical simulations [24] in the dressed state basis, which is a well-known approach for studying standing wave excitation [25,26]. The simulations do not include the effect of atomic recoil. In this model, as the pulse width increases, the atoms experience damped harmonic mo-

tion and channeling into the nodes of the standing wave potential. As a result, the atoms sample different portions of the spatially varying potential, which causes small changes in the populations of the dressed states. The motion also causes a mixing of dressed states within in a single manifold. The effective radiative rate is the sum of two radiative rates, one for each transition from the mixed state to the dressed states in the next lower manifold. This rate can be shown to be position dependent and this dependence is caused by the variation in the field intensity due to the standing wave potential and the spatial profile of the excitation beams. By studying the evolution of 2.5×10^4 atoms, we find that the effective radiative rate increases as a function of pulse duration and exhibits an oscillatory behavior related to the motion in the standing wave potential. The effective rate also approaches an asymptotic value for the range of τ_2 used in the experiment. However, the variation in the effective radiative rate is only $\sim$10% of the range shown in Fig. 18. The simulations also show a dependence on Rabi frequency that is not observed in the experiment. We conclude that a more complete theoretical understanding is necessary to explain the measured dependence of the radiative rate on τ_2.

V. CONCLUSIONS

We have presented a detailed study of the dependence of the echo envelope and echo amplitude on Δk, atom-field coupling, spatial profile, and spontaneous emission. All these effects have a significant impact on high precision measurements of ω_r using this technique. This work also shows that the simplified treatment of the echo signal in Eq. (18) [10] is not sufficient to understand the details of the signal shape and for carrying out precision measurements. We have observed a variation in the radiative rate as a function of the interaction time of the second excitation pulse, an interesting effect that can be fully interpreted based on improved theoretical understanding.

We have reported a precision measurement of the recoil frequency precise to 2.5 ppm based on the AI discussed in this paper [11]. The time scale of the experiment was $\sim$10 ms and the results showed reduced sensitivity to a range of systematic effects compared other AIs. This work allows us to undertake measurements of the recoil frequency on a time scale of $\sim$100 ms using an expanded interaction region and further extending the time scale in a fountain for achieving a competitive measurement. This has been an area of active research since many high profile experiments have recently demonstrated precision measurements of the fine structure constant α at the level of 10 parts per 10^9 (ppb) or better. These include the most precise atom interferometric measurement [2] (precise to 7.4 ppb) as well as the most precise noninterferometric measurement using cold atoms [27] which has attained a precision of 6.7 ppb. Other recent measurements of α are based on Helium spectroscopy (precise to 10 ppb) [28]. The goal of these measurements is to provide independent tests of quantum electrodynamics by measuring α at the same level of precision as the improved electron g factor measurement [29,30] that was recently reported.

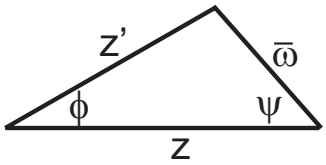

FIG. 19. Geometry.

The AI discussed in this paper is an independent technique that has the potential for obtaining a measurement of α precise to a few ppb. The primary requirements for completing the measurement that is underway are the elimination of magnetic field gradients and increasing the size of the interaction region.

ACKNOWLEDGMENTS

This work was supported by Canada Foundation for Innovation, Ontario Innovation Trust, National Sciences and Engineering Research Council, Photonics Research Ontario, and York University. We would like to thank Boris Dubetsky, Paul Berman, and Helen Freedhoff for helpful discussions.

APPENDIX

Here we describe the steps involved to modify the identity 11 to allow for complex arguments. We start with the generating function [17,31]

$$e^{\phi/2(t-1/t)}=\sum_{n=-\infty}^{\infty}t^nJ_n(\phi). \tag{A1}$$

If $t=ie^{iqx}$, then $t-t^{-1}=2i\cos(qx)$ and Eq. (A1) becomes

$$e^{i\phi\cos(qx)}=\sum_{n=-\infty}^{\infty}i^nJ_n(\phi)e^{inqx}. \tag{A2}$$

Now, using the Bessel function identity

$$J_\nu(\bar{\omega})\left[\frac{z-z'e^{-i\phi}}{z-z'e^{i\phi}}\right]^{\nu/2}=\sum_{l=-\infty}^{\infty}J_{l+\nu}(z)J_l(z')e^{il\phi}, \tag{A3}$$

where

$$\bar{\omega}=\sqrt{z^2+z'^2-2zz'\cos\phi}, \tag{A4}$$

implying the geometry shown in Fig. 19. We can see from this geometry that

$$z-z'\cos\phi=\bar{\omega}\cos\psi, \tag{A5a}$$

$$z'\sin\phi=\bar{\omega}\sin\psi, \tag{A5b}$$

and therefore

$$\frac{z-z'e^{-i\phi}}{z+z'e^{i\phi}}=\frac{\bar{\omega}\cos\psi+i\bar{\omega}\sin\psi}{\bar{\omega}\cos\psi-i\bar{\omega}\sin\psi}=e^{2i\psi} \tag{A6}$$

and Eq. (A3) becomes

$$e^{i\nu\psi}J_\nu(\bar{\omega}) = \sum_{l=-\infty}^{\infty} J_{l+\nu}(z)J_l(z')e^{il\phi}. \tag{A7}$$

The situation for summing pairs of Bessel functions with the same argument can be visualized on the basis of an isosceles triangle with equal interior angles ψ and equal sides $z=z'=u$. In this case

$$\bar{\omega} = u\sqrt{2(1-\cos\phi)} = 2u\sin(\phi/2), \tag{A8}$$

so that Eq. (A7) becomes

$$J_\nu(2u\sin(\phi/2)) = e^{-i\nu\psi}\sum_{l=-\infty}^{\infty} J_{l+\nu}(u)J_l(u)e^{il\pi}e^{-2il\psi}. \tag{A9}$$

We are interested in the case where the arguments of the Bessel functions z and z' are complex and defined by $z=ue^{-i\theta}$ and $z'=ue^{i\theta}$, where u and θ are defined by Eqs. (20) and (21), respectively. Equation (A4) is then modified as

$$\bar{\omega} = 2u\sqrt{\sin(\phi/2+\theta)\sin(\phi/2-\theta)} \tag{A10}$$

and Eqs. (A5a) and (A5b) can be combined to give

$$2iue^{-i\phi/2}\sin(\phi/2-\theta) = \bar{\omega}e^{i\psi}. \tag{A11}$$

Algebraic manipulation of Eq. (A11) gives

$$e^{i\psi} = ie^{-i\phi/2}\sqrt{\frac{\sin(\phi/2-\theta)}{\sin(\phi/2+\theta)}} \tag{A12}$$

and Eq. (A9) becomes

$$i^\nu J_\nu[\bar{\omega}]\left[\frac{\sin(\phi/2-\theta)}{\sin(\phi/2+\theta)}\right]^{\nu/2} = \sum_{l=-\infty}^{\infty} e^{i\nu\phi/2}J_{l+\nu}(ue^{-i\theta})J_l(ue^{i\theta})e^{il\phi}. \tag{A13}$$

[1] *Atom Interferometry*, edited by P. R. Berman (Academic Press, San Diego, 1997).
[2] A. Wicht, J. M. Hensley, E. Sarajlic, and S. Chu, Phys. Scr., T **102**, 82 (2002).
[3] D. S. Weiss, B. C. Young, and S. Chu, Phys. Rev. Lett. **70**, 2706 (1993).
[4] A. Peters, K. Y. Chung, and S. Chu, Nature (London) **400**, 849 (1999).
[5] T. L. Gustavson, P. Bouyer, and M. A. Kasevich, Phys. Rev. Lett. **78**, 2046 (1997).
[6] J. M. McGuirk, G. T. Foster, J. B. Fixler, M. J. Snadden, and M. A. Kasevich, Phys. Rev. A **65**, 033608 (2002).
[7] D. Schneble, Y. Torii, M. Boyd, E. W. Streed, D. E. Pritchard, and W. Ketterle, Science **300**, 475 (2003).
[8] E. W. Hagley *et al.*, Phys. Rev. Lett. **83**, 3112 (1999).
[9] G. K. Campbell, A. E. Leanhardt, J. Mun, M. Boyd, E. W. Streed, W. Ketterle, and D. E. Pritchard, Phys. Rev. Lett. **94**, 170403 (2005).
[10] S. B. Cahn, A. Kumarakrishnan, U. Shim, T. Sleator, P. R. Berman, and B. Dubetsky, Phys. Rev. Lett. **79**, 784 (1997).
[11] M. Weel, S. Beattie, I. Chan, E. Rotberg, A. Vorozcovs, and A. Kumarakrishnan (to be published).
[12] M. Weel, I. Chan, S. Beattie, A. Kumarakrishnan, D. Gosset, and I. Yavin, Phys. Rev. A **73**, 063624 (2006).
[13] M. Weel and A. Kumarakrishnan, Phys. Rev. A **67**, 061602(R) (2003).
[14] S. B. Cahn, Ph.D. thesis, SUNY Stony Brook, 1997.
[15] M. Weel, Ph.D. thesis, York University, 2005.
[16] D. V. Strekalov, A. Turlapov, A. Kumarakrishnan, and T. Sleator, Phys. Rev. A **66**, 023601 (2002).
[17] G. Arfken and H. Weber, *Mathematical Methods for Physicists* (Harcourt, London, UK, 2001).
[18] P. L. Gould, G. A. Ruff, and D. E. Pritchard, Phys. Rev. Lett. **56**, 827 (1986).
[19] S. Gupta, K. Dieckmann, Z. Hadzibabic, and D. E. Pritchard, Phys. Rev. Lett. **89**, 140401 (2002).
[20] B. Dubetsky (private communication).
[21] J. E. Simsarian, L. A. Orozco, G. D. Sprouse, and W. Z. Zhao, Phys. Rev. A **57**, 2448 (1998).
[22] E. A. Rotberg, B. Barrett, S. Beattie, S. Chudasama, M. Weel, I. Chan, and A. Kumarakrishnan, J. Opt. Soc. Am. B **24**, 671 (2007).
[23] A. Vorozcovs, M. Weel, S. Beattie, S. Cauchi, and A. Kumarakrishnan, J. Opt. Soc. Am. B **22**, 943 (2005).
[24] B. Barrett, S. Beattie, and A. Kumarakrishnan, Bull. Am. Phys. Soc. **52**, 53 (2007).
[25] J. Dalibard and C. Cohen-Tannoudji, J. Opt. Soc. Am. B **2**, 1707 (1985).
[26] J. Chen, J. G. Story, and R. G. Hulet, Phys. Rev. A **47**, 2128 (1993).
[27] P. Cladé, E. de Mirandes, M. Cadoret, S. Guellati-Khélifa, C. Schwob, F. Nez, L. Julien, and F. Biraben, Phys. Rev. Lett. **96**, 033001 (2006).
[28] T. Zelevinsky, D. Farkas, and G. Gabrielse, Phys. Rev. Lett. **95**, 203001 (2005).
[29] G. Gabrielse, D. Hanneke, T. Kinoshita, M. Nio, and B. Odom, Phys. Rev. Lett. **97**, 030802 (2006).
[30] B. Odom, D. Hanneke, B. D'Urso, and G. Gabrielse, Phys. Rev. Lett. **97**, 030801 (2006).
[31] G. N. Watson, *A Treatise on the Theory of Bessel Functions* (Cambridge Univeristy Press, New York, 1944).